

Article

Wake Structures and Hydrodynamic Characteristics of Flows around Two Near-Wall Cylinders in Tandem and Parallel Arrangements

Xing Chang ¹, Pandeng Yin ², Jianjian Xin ^{2,*}, Fulong Shi ³ and Ling Wan ² 

¹ State Key Laboratory of Maritime Technology and Safety, Shanghai Ship and Shipping Research Institute Co., Ltd., Minsheng Rd. 600, Shanghai 200135, China; changxing90@126.com

² Institute of Naval Architecture and Ocean Engineering, Ningbo University, Ningbo 315211, China; yinpandeng@outlook.com (P.Y.); wanling@nbu.edu.cn (L.W.)

³ School of Shipping and Naval Architecture, Chongqing Jiaotong University, Chongqing 400074, China; shifulongk@163.com

* Correspondence: xinjianjian@nbu.edu.cn

Abstract: To clarify the hydrodynamic interference characteristics of flows around multiple cylinders under the wall effect, the two-dimensional (2D) flows around the near-wall single, two tandem and parallel cylinders are simulated under different gap ratios ($0.15 \leq G/D \leq 3.0$) and spacing ratios ($1.5 \leq T/D \leq 4.0$) at a Reynolds number of $Re = 6300$. We also examine the wake patterns, the force coefficients, and the vortex-shedding frequency with emphases on the wall effect and effects of the two-cylinder interference. A critical wall gap of $G/D = 0.6$ is identified in the single-cylinder case where the wall can exert significant influences. The two near-wall tandem cylinders exhibit three wake states: stretching mode, attachment mode, and impinging mode. The force coefficients on the upstream cylinder are significantly affected by the wall for $G/D \leq 0.6$. The downstream cylinder is mainly influenced by the upstream cylinder. For $G/D > 0.6$, the force coefficients on the two cylinders exhibit a similar variation trend. In the parallel arrangement, the two cylinders exhibit four wake states in different G/D and T/D ranges: double stretching mode, hetero-vortex scale mode, unilateral vortex mode, and free vortex mode. Moreover, the two parallel cylinders in the hetero-vortex scale or free vortex mode have two states: synchronous in-phase state and synchronous out-of-phase state. The mean drag coefficients on the two cylinders decrease, while the mean lift coefficients exhibit opposite variation trends, as the T/D grows.

Keywords: two tandem cylinders; parallel cylinders; wall effects; wake patterns; interference effect



Citation: Chang, X.; Yin, P.; Xin, J.; Shi, F.; Wan, L. Wake Structures and Hydrodynamic Characteristics of Flows around Two Near-Wall Cylinders in Tandem and Parallel Arrangements. *J. Mar. Sci. Eng.* **2024**, *12*, 832. <https://doi.org/10.3390/jmse12050832>

Academic Editors: Spyros A. Mavrakos and Dimitrios N. Konispoliatis

Received: 11 April 2024

Revised: 6 May 2024

Accepted: 11 May 2024

Published: 16 May 2024



Copyright: © 2024 by the authors. Licensee MDPI, Basel, Switzerland. This article is an open access article distributed under the terms and conditions of the Creative Commons Attribution (CC BY) license (<https://creativecommons.org/licenses/by/4.0/>).

1. Introduction

The flow around cylinders near a wall has extensive engineering applications, such as water supply, sewage pipes serving coastal cities, oil and gas pipelines laid under the seabed, as well as submarine optical cables [1,2]. Due to seawater erosion, gaps can be formed between the subsea pipeline and the seabed, resulting in cantilevered cylindrical structures. Under the action of the ocean current, the periodic vortex-shedding phenomenon will occur behind the submarine pipeline, which can induce fatigue failure, thereby reducing the operational longevity of the pipeline [3]. In addition, the existence of the seabed and the hydrodynamic interference between adjacent pipelines can have severe influences on the wake mode and dynamic response patterns of the cylinders. As a consequence, the environment becomes more complex and is more prone to fatigue damage.

In the past few decades, flows around cylinders have been extensively investigated by experiments [4,5] and the numerical method [6,7]. For example, Duan and Wan [8] numerically analyzed the wake characteristics of flows around a circular cylinder at $Re = 3900$. They demonstrated that the velocity profile in the wake region exhibited “U” patterns and

“V” patterns. Manzoor et al. [9] numerically studied the flow around a triangular cylinder by a lattice Boltzmann method (LBM). They analyzed the variation of the vortex structures and force coefficients with the Reynolds number. Also, Aksoy et al. [10] investigated the flow around a circular cylinder by experimental measurements combining with the machine-learning method. With respect to the multiple cylinders, Lam et al. [11] experimentally studied the flows around four cylinders in a square arrangement at the Reynolds number of $Re = 200$. Some typical wake features were identified depending on the angles of incidence. Niegodajew et al. [12] experimentally investigated the flow around two bluff bodies in a tandem arrangement. They focused on the influence of the gap spacing between the two cylinders on the flow patterns. Mishra and Sen [13] numerically simulated the flow around two tandem rectangular cylinders by a finite element method. They found two transitions of the vortex-shedding mode with the variation of the gap spacing.

Nowadays, there have been abundant achievements concerning flows around the cylinders from multiple aspects, such as the different Reynolds numbers [9,14], conditions of incoming flow [15], section shapes [5,6,14] and geometric arrangements [16–18]. Comprehensive research achievements can refer to many specialized topic reviews [19–26]. However, the available results mostly concentrate on the free flow boundary problems. Studies on near-wall flows around the cylinders are relatively scarce. The existence of a wall can measurably affect the vibration response and wake patterns of cylinders. It exhibits new features, such as asymmetric loading, gap flow, vortex-shedding suppression and wall vortex roll-up. In addition, the shear layer and wake interference between multiple cylinders, especially the complex gap flow deflection phenomenon under small spacings, makes the flow mechanism more complicated.

On account of the near-wall flows around a cylinder, Ouro et al. [27] demonstrated that the near-wall effect can lead to the lifting of the wake around the near-wall cylinder. Zhou et al. [28] experimentally investigated the influence of the gap ratio (G/D) in the flows around a single cylinder close to a wall at $Re = 200$. They found that the near-wall effect of the cylinder on the flow characteristics was almost not observed for $G/D > 0.6$. Zhang et al. [29] simulated near-wall flows at a low Reynolds number for $G/D = 0.4$. It was shown that increasing the thickness ratio of the boundary layer would weaken the wall effect and reduce the vortex-shedding frequency. Zhou et al. [30] experimentally examined the flows around a cylinder at $Re = 1000$ for $G/D = 0.5$ and 1. It was found that secondary vortices would be formed periodically on the wall. The intensity of the vortices shedding from the upper surface of the cylinder is slightly greater than that from the lower surface. In addition, Zhai et al. [31] experimentally investigated the effects of the wall spacing on the flow patterns of a single near-wall cylinder at $Re = 300$. They concluded that the instability of the near-wall region was mainly caused by the alternative vortex shedding of the wake. Li et al. [32] numerically investigated the Honji instability of a cylinder near a flat wall. They found that the Honji instability is mainly generated on the gap side of the cylinder. Other investigations regarding the near-wall flow include the different shape of the cylinder [33,34], compressible flow [35], and two circular cylinders [36,37].

The above-mentioned research [27–35] mainly focuses on the near-wall flows around a single cylinder. The studies on the near-wall flow around multiple cylinders are rare. However, in the field of oil and gas transportation, the configuration of multiple cylinders is usually adopted. Two cylinders in tandem and parallel arrangements provide a simple multi-body model. In the available investigations, Li et al. [36] numerically simulated the near-wall flow around two tandem circular cylinders by OpenFOAM with the consideration of three small gap ratios between the cylinder and the wall. Liu et al. [37] experimentally investigated the flow around two parallel circular cylinders. They examined the influence of the central spacings between the two cylinders on the wake patterns. The dynamic characteristics are not yet discussed. Currently, near-wall flows around the multiple cylinders exert abundant phenomena yet to be fully understood. There remains a lack of comprehensive studies on the influence of key factors such as the flow conditions, the arrangement form, and the gap spacing. Especially, the vortex-shedding mode and

dynamic response features of the cylinders, under the interaction of the gap flow and the wake flow, have not been thoroughly investigated. This paper numerically investigates the two-dimensional (2D) flows around a single cylinder and the two tandem and parallel cylinders close to a wall. The different gap ratios and cylinder spacing ratios are considered with a constant Reynolds number of $Re = 6300$. We analyzed the wake modes, the force coefficients, and the vortex-shedding frequencies under the near-wall effects and the hydrodynamic interference of two cylinders. This study is expected to provide a new understanding of the near-wall flow phenomena. Also, it is of practical significance to realize effective flow control for mitigating structural fatigue.

2. Mathematical Formulation

The 2D flows around one and two near-wall circular cylinders are simulated in this study. Figure 1 presents the geometric model and the boundary conditions in the considered computational domains. The incompressible, viscous flow is assumed. The wall and the cylinder surface are assumed to be no-slip. The governing equations for the incompressible viscous flow adopted are the 2D Reynolds-averaged Navier–Stokes (RANS) equations. The RANS model can well consider the effects of the turbulent flows, while the required computational resources are much less than required by the large eddy simulation (LES) model. The dimensionless form of the governing equations is expressed in the Cartesian coordinate system as follows:

$$\frac{\partial u_i}{\partial x_i} = 0 \tag{1}$$

$$\frac{\partial u_i}{\partial t} + u_j \frac{\partial u_i}{\partial x_j} + \frac{\partial p}{\partial x_i} - \frac{1}{Re} \frac{\partial}{\partial x_j} \left[\frac{\partial u_i}{\partial x_j} + \frac{\partial u_j}{\partial x_i} \right] - \frac{\overline{\partial u_i^* u_j^*}}{\partial x_j} = 0 \tag{2}$$

$$\frac{\partial u}{\partial y} = 0, v = 0$$

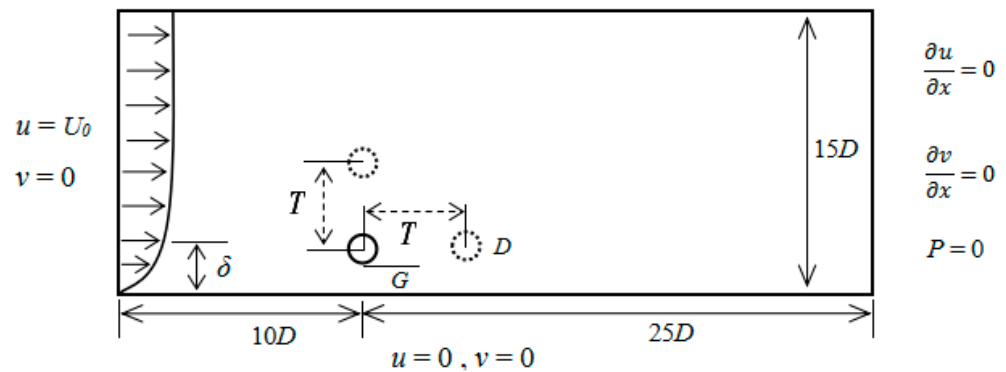


Figure 1. Geometric model and boundary conditions.

The normalization of Equations (1) and (2) is realized based on the diameter of the cylinder D and the free-stream velocity of U_0 at the inlet, as shown in Figure 1. Therefore, the important flow parameter of the Reynolds number can be obtained with $Re = U_0 D / \nu$. In Equation (2), $\overline{u_i^* u_j^*}$ is the Reynolds stress tensor, which is expressed as:

$$-\overline{u_i^* u_j^*} = \mu_t \left[\frac{\partial u_i}{\partial x_j} + \frac{\partial u_j}{\partial x_i} \right] - \frac{2}{3} k \delta_{ij} \tag{3}$$

The standard $k-\varepsilon$ model is adopted for the simulations of fully turbulent flows. This $k-\varepsilon$ model has a good convergence rate and requires relatively low memory. Moreover, it performs well in solving external flow problems with complex geometries. It is given as:

$$\frac{\partial k}{\partial t} + u_j \frac{\partial k}{\partial x_j} = \frac{\partial}{\partial x_j} \left[\left(\nu + \frac{\mu_t}{\sigma_k} \right) \frac{\partial k}{\partial x_j} \right] + \mu_t \left[\frac{\partial u_i}{\partial x_j} + \frac{\partial u_j}{\partial x_i} \right] \frac{\partial u_i}{\partial x_j} - \varepsilon \quad (4)$$

$$\frac{\partial \varepsilon}{\partial t} + u_j \frac{\partial \varepsilon}{\partial x_j} = \frac{\partial}{\partial x_j} \left[\left(\nu + \frac{\mu_t}{\sigma_\varepsilon} \right) \frac{\partial \varepsilon}{\partial x_j} \right] + C_1 \frac{\varepsilon}{k} \mu_t \left[\frac{\partial u_i}{\partial x_j} + \frac{\partial u_j}{\partial x_i} \right] \frac{\partial u_i}{\partial x_j} - C_2 \frac{\varepsilon}{k} \quad (5)$$

The turbulent viscosity coefficient is given as $\mu_t = C_\mu k^2 / \varepsilon$. The coefficients of the standard $k-\varepsilon$ model are determined according to Launder and Spalding [38]:

$$C_1 = 1.44, \quad C_2 = 1.92, \quad \sigma_k = 1.0, \quad \sigma_\varepsilon = 1.3, \quad C_\mu = 0.09. \quad (6)$$

The drag coefficient C_d , the lift coefficient C_l , and the Strouhal number St are the critical dimensionless parameters. They are given as follows:

$$C_d = \frac{F_d}{0.5\rho U_0^2 D}, \quad C_l = \frac{F_l}{0.5\rho U_0^2 D} \quad (7)$$

$$St = \frac{fD}{U_0} \quad (8)$$

3. Numerical Method

3.1. Numerical Implementation

The present computational model is established based on the software of STAR-CCM+ 13.04. The RANS model is adopted to solve the flow patterns around the cylinders with the standard $k-\varepsilon$ model for consideration of the turbulence characteristics. The overlapping grid is used to treat the solid boundaries. The governing equations are discretized by the finite volume method. The convective and the viscous terms are approximated by the second-order upwind and central differencing schemes, respectively. The second-order implicit scheme is used to advance the governing equation in time. The semi-implicit method for pressure-linked equations (SIMPLE) method is employed to decouple the velocity and pressure. To ensure the good convergence and stability of the calculation, we set the pressure relaxation factor to 0.3 and the velocity relaxation factor to 0.7.

3.2. Geometric Models and Boundary Condition

The width of the computational domain is set as $15 D$. The center of the cylinder is positioned $10 D$ from the inlet and $25 D$ from the outlet. The thickness ratio of the boundary layer is given as $\delta/D = 0.2$. Also, the gap ratio between the cylinder center and the wall G/D is chosen from 0.15 to 3.0. The spacing ratio of two cylinders in the tandem and parallel arrangement T/D is from 1.5 to 4. The primary intention of this study is to investigate the influence of the gap ratio and spacing ratio on the wake pattern and dynamic characteristics. Therefore, a fixed Reynolds number is adopted with $Re = 6300$, though the Reynolds number is the critical flow parameter affecting the flow characteristics. In addition, the flow is usually in the sub-critical regime, where the Reynolds number ranges from 300 to 1.4×10^5 [39]. The Reynolds number of $Re = 6300$ adopted is consistent with the realistic situation in engineering, and the requirement for the computational resource is acceptable. Also, there are experimental studies [40] available for comparison. In terms of the boundary conditions, the uniform inflow boundary condition with a velocity of U_0 is enforced on the inlet. The outlet is set as the pressure outlet boundary condition. The cylindrical surface and the lower wall are prescribed as no-slip wall boundary conditions. In addition, a slip wall boundary condition is imposed on the upper wall. Regarding the turbulence parameters, the turbulent kinetic energy k and the turbulence dissipation rate ε

are applied. They are estimated through the formulae of $k = 1.5(U_0 I)^2$ and $\epsilon = C^{0.75} k^{1.5} / D$, where I is the turbulence intensity dependent on the Reynolds number, and C is generally taken as 0.09.

3.3. Grid Generation

A structured grid is adopted to separate the computational domain into four regions, and the local grid around the cylinder is shown in Figure 2. To examine the grid independence, three grids with different resolutions are considered. Detailed information on three grids is presented in Table 1. The grid NO. 1 has approximately 54,000 elements. The grid NO. 2 is refined based on the grid NO. 1, with the element number of around 190,000. Also, the grid NO. 3 is further refined based on the grid NO. 2, with the element number of about 540,000.

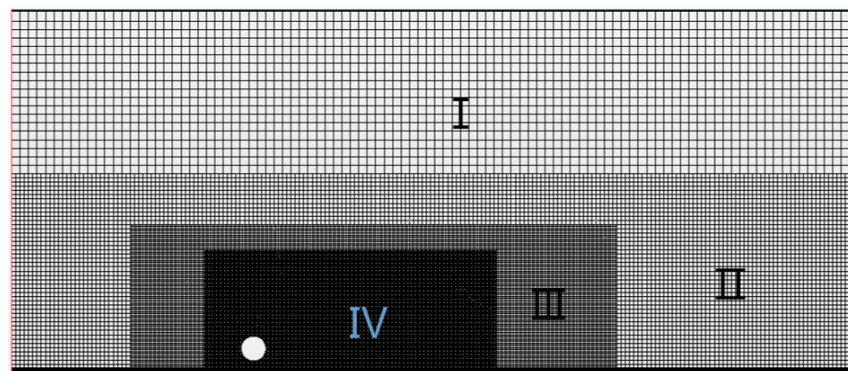


Figure 2. Local grid division around the near-wall cylinder.

Table 1. Detailed information on the three grids.

Grid Resolutions	Grid NO. 1	Grid NO. 2	Grid NO. 3
Grid size of region I/mm	3.5	3.5	3.5
Grid size of region II/mm	1.6	0.8	0.8
Grid size of region III/mm	0.8	0.4	0.4
Grid size of region IV/mm	0.4	0.2	0.1
Number of elements	53,721	190,642	540,170

3.4. Grid Independence Verification

The flow around a near-wall cylinder with a gap distance of $G/D = 0.5$ at $Re = 6300$ is simulated to test the grid independence. The three grids are presented in Table 1. The time step is set as 0.002 s to ensure the good stability of the simulation. Table 2 presents the predicted average drag coefficient \bar{C}_d , the average lift coefficient \bar{C}_l , and the Strouhal number St of the three grids, in comparison with the reference results.

The results, including the force coefficients and the Strouhal number, are very close for the three grids, confirming the good grid convergence. Reasonably good agreements with the reference results have been obtained, which validates the accuracy of the present numerical model. Specifically, the \bar{C}_d of the three grids is very close to the 1.02 obtained in Wang et al.'s [40] experiment. The \bar{C}_l approaches the 0.13 in Wang et al.'s experiment [40] and is also consistent with the 0.137 gained in Lei et al.'s experiment [41]. In terms of the St , it agrees well with that in Lei et al.'s experiment [41] and Kazeminezhad et al.'s numerical method [42]. In the following cases, the grid NO. 2 is adopted to achieve a good balance between the computational resources and the solution quality.

Table 2. Comparison of the force coefficients and the Strouhal number on the near-wall cylinder at $Re = 6300$.

Numerical Method	\bar{C}_d	\bar{C}_l	St
Grid NO. 1	1.04	0.130	0.24
Grid NO. 2	1.05	0.140	0.23
Grid NO. 3	1.10	0.133	0.23
Wang et al. [40]	1.02	0.13	0.195
Kazeminezhad et al. [42]	1.13	0.116	0.233
Lei et al. [41]	1.30	0.137	0.21

4. Numerical Results and Discussion

4.1. Near-Wall Single Cylinder

In this section, the flows around a single cylinder adjacent to a wall are studied. In particular, the influence of G/D on the dynamic characteristics and wake mode is analyzed. Figure 3 shows the time history of the lift (C_l) and drag (C_d) coefficients on the single cylinder for different G/D . For $G/D \leq 0.2$, C_l and C_d approach a constant value after several periods of initial disturbance. No regular oscillation is observed, indicating that the wall inhibits the generation of vortex shedding. For $G/D \geq 0.3$, sinusoidal oscillation patterns are observed, because periodic shedding vortices are generated on the cylindrical surface. As the cylinder stays away from the wall ($0.3 \leq G/D \leq 0.6$), the undulation amplitude of C_l increases, because the intensity of vortex shedding grows. For a larger gap ratio of $G/D > 0.6$, the amplitude of C_l starts to decrease. The influence of the wall on the cylinder begins to weaken, which is consistent with the experimental conclusion of Zhou et al. [28].

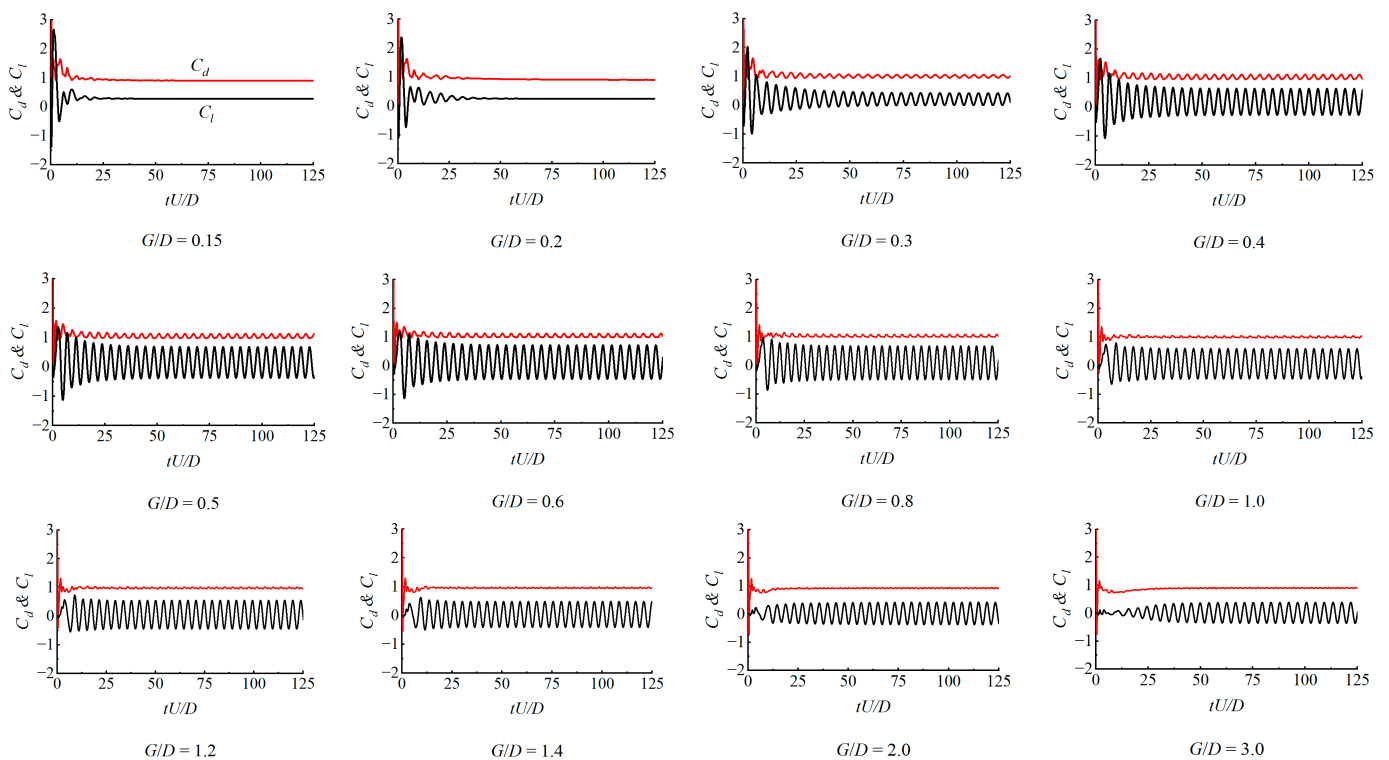


Figure 3. Time history of the drag and lift coefficients on a single near-wall cylinder at $Re = 6300$ for different G/D .

The average drag and lift coefficients of \bar{C}_d and \bar{C}_l for the single cylinder at different G/D are demonstrated in Figure 4. The average force coefficients predicted by the present method for various gap ratios are in satisfactory agreement with previous work [40–42]. As the G/D rises, the \bar{C}_d grows to maximum for $G/D = 0.6$ following by a gradual decrease. In contrast, the \bar{C}_l decreases dramatically for $G/D < 1.5$ and then shows a slow downward trend as the G/D further reduces. Note that the \bar{C}_d predicted by the present method is slightly smaller than that predicted by the previous methods [40–42] for most gap ratios. These discrepancies may be caused by the different boundary layer thicknesses δ/D . In the study by Wang et al. [40], $\delta/D = 0.47$. It is set as $\delta/D = 0.25$ in Lei et al. [41] and $\delta/D = 0.3$ in Kazeminezhad et al. [42]. The boundary layer thickness is an important variable that cannot be ignored. According to the conclusions of Kazeminezhad et al. [42], the \bar{C}_d can be noticeably affected by the δ/D . The reasons for this are that the flow velocity on the cylinder is not constant in different boundary layers at a specific gap ratio. In other words, the velocity close to the cylinder surface would vary with the δ/D . In addition, the Reynolds number (Re) adopted in this paper is also different from that used in Lei et al. [41] and Kazeminezhad et al. [42], which may also cause the difference in the numerical results. Generally, the present \bar{C}_d and \bar{C}_l agree well with the experimental and numerical results, which validates the reliability of the present numerical method.

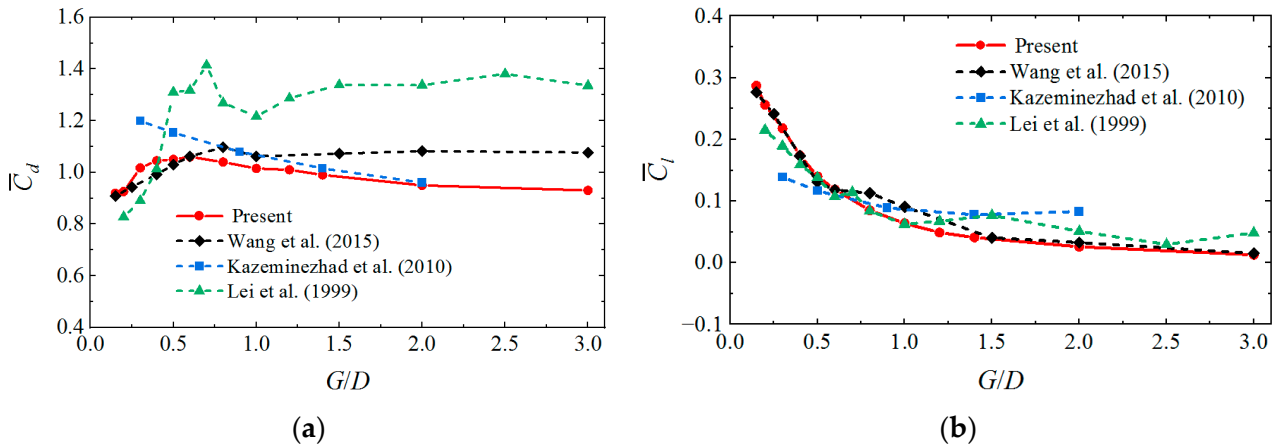


Figure 4. The mean force coefficients on a single near-wall cylinder at $Re = 6300$ for different G/D : (a) mean drag coefficient; and (b) mean lift coefficient [40–42].

The distributions of the pressure coefficient on the cylindrical surface for different G/D are presented in Figure 5, where the counterclockwise rotation is defined as positive and the clockwise rotation is negative. They are compared with the reference results [43–45]. The angle is varied with an increment of 30° . In Figure 5a, the pressure coefficient behind the rear part of the cylinder ($-90 < \theta < 90$) is significantly smaller than that on the front side. This is due to the direct impinging of the incoming flow on the front side of the cylinder. Consequently, an apparent high-pressure area is generated on the front side of the cylinder, and a negative pressure area is created behind the cylinder. For $G/D \leq 0.2$, the velocity of the incoming flow impinging on the cylindrical surface decreases due to the inhibition effects of the wall, which reduces the pressure differences between the front and rear sides of the cylinder. The pressure distributions for $G/D \geq 0.6$ nearly coincide because the wall effects are weakened. Also, the pressure exerted on the lower side of the cylinder is less than that on the upper side, generating a positive transverse force. The calculated pressure coefficients for three gap ratios of $G/D = 0.4, 0.6,$ and 0.8 are compared with the experimental data [43] and the simulation results [44,45] in Figure 5b. They are consistent with the experimental and the simulation results, again confirming the reliability of the numerical model.

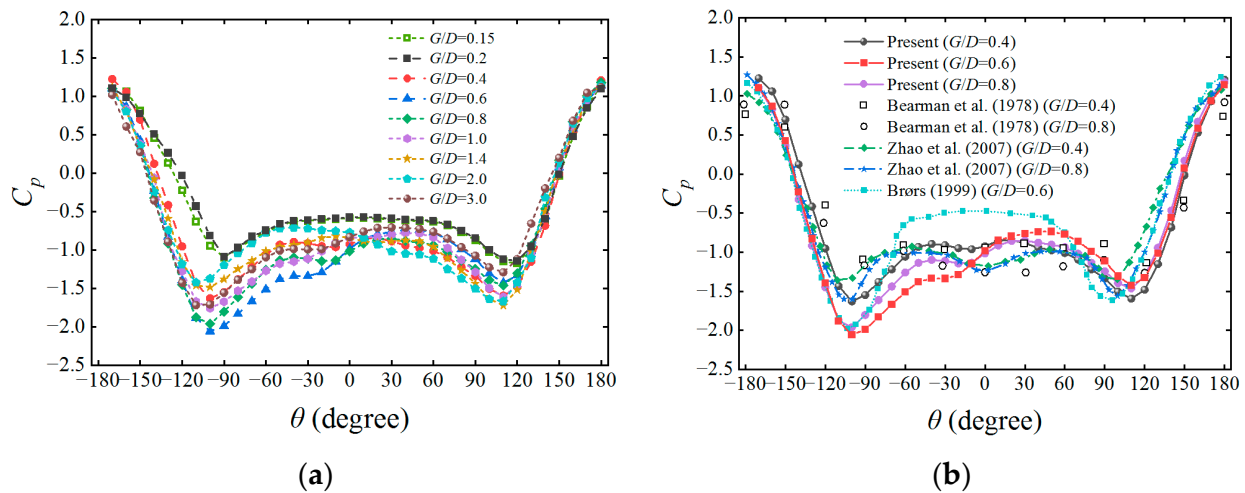


Figure 5. Distributions of the pressure coefficient on the cylindrical surface at $Re = 6300$ for different G/D : (a) present results for different G/D ; and (b) comparison with the reference results [43–45].

Furthermore, the influence of the wall effects on the separation angle is discussed. As shown in Figure 5a, the position of 0° is at the rear stagnation point of the cylinder, and the position of 180° or -180° represents the front stagnation point. The separation angle can be determined by the front stagnation point, the separation point, and the center of the cylinder. It is seen in Figure 5a that the inflection point of the pressure distribution maintains at approximately 95° on the upper surface of the cylinder. Therefore, the separation angle on the upper surface is determined to be about 85° for various gap ratios. The results are consistent with those of the flows around a single cylinder by Kravchenko et al. [46] and Franke et al. [47], again confirming the accuracy of the present model. However, the separation angle on the lower surface of the cylinder is not symmetrical with that on the upper surface. The separation angle on the lower surface is about 105° for $G/D = 0.2$ and 0.15 , and it is around 95° for $G/D \geq 0.4$. It is indicated that the presence of the wall effect can cause the delay of the separation point. Moreover, the smaller the gap ratio, the more significant the influence on the separation point due to the greater intensity of the wall effect.

4.2. Two Near-Wall Tandem Cylinders

This section simulates flows around two tandem cylinders near a wall at $Re = 6300$ to examine the wall effect and hydrodynamic interaction by changing the gap ratio (G/D) and the spacing ratio (T/D). The vorticity contours around the cylinders under different G/D and T/D are studied first, as presented in Figure 6. For $G/D = 0.2$, the wall suppresses the generation of the vortices from the two cylinders at different T/D . Therefore, the upper shear layer on the upstream cylinder is reattached on the downstream one, forming an elongate shear layer to extend downstream. When G/D is larger than 0.4 , a vortex near the wall is generated and interacts with the one generated from the upper cylinder. The large-scale vortex is then formed to travel downstream. As the gap ratio grows, the generation location of the wall vortex moves backward. In real sea conditions, the wall vortices can be generated by the seabed surface. Moreover, they can carry the sand particles to the low-speed area behind the cylinder due to the upward migration. The sand particles would deposit in this low-speed area due to the limitation of velocity. Gradually, a sand accumulation line is formed.

Accounting for the influence of the T/D , the alternative vortex shedding of the upstream cylinder cannot be developed for $T/D = 1.5$ since the downstream cylinder suppresses the detachment of the shear layers. As a result, the wake pattern of the two cylinders is in an extended state, showing a stretching mode. For $T/D = 3$, vortex pairs start to appear between the two cylinders, and no vortex shedding occurs. The shear layer of the upstream

cylinder will adhere to the front side of the downstream one, showing an attachment mode. For $T/D = 4$, an alternative vortex-shedding phenomenon occurs between the two cylinders at $G/D \geq 0.4$. The shedding vortices will impact the front side of the downstream cylinder, showing an impinging mode. Compared with $T/D = 3$, it is shown that the upper shear layer of the downstream cylinder is elongated and enlarged.

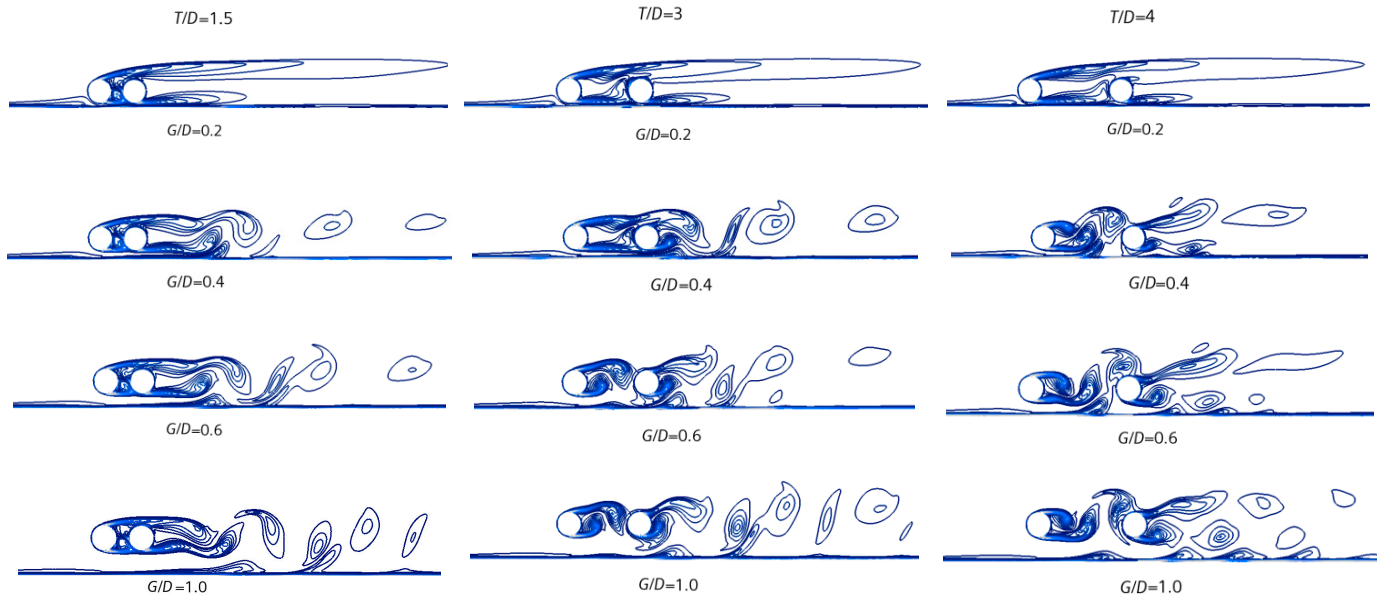


Figure 6. Instantaneous vorticity contours around the two tandem cylinders at $Re = 6300$ with different G/D and T/D .

Figure 7 illustrates the time history of the lift (C_l) and drag (C_d) coefficients on two cylinders at $T/D = 3$. The oscillation amplitudes of both C_l and C_d on the downstream cylinder are much larger than those on the upstream one. This is because the vortex shedding from the upper cylinder enhances the vorticity intensity of the downstream one. At $G/D = 0.4$, steady force coefficients are obtained after several periods of initial disturbance, since the alternative vortex shedding is inhibited. The C_l on the upstream cylinder approaches to the steady state after a dimensionless time of 60. In contrast, the oscillation amplitude of the C_l on the downstream cylinder will gradually increase again until it reaches stability. In this situation, the shedding vortex of the upstream cylinder is restrained. The shear layers of the two cylinders are in a stretching state and begin to produce a single vortex street. As the gap spacing further increases to $G/D \geq 0.6$, the C_l on two cylinders exhibits a sinusoidal oscillation pattern after initial disturbance.

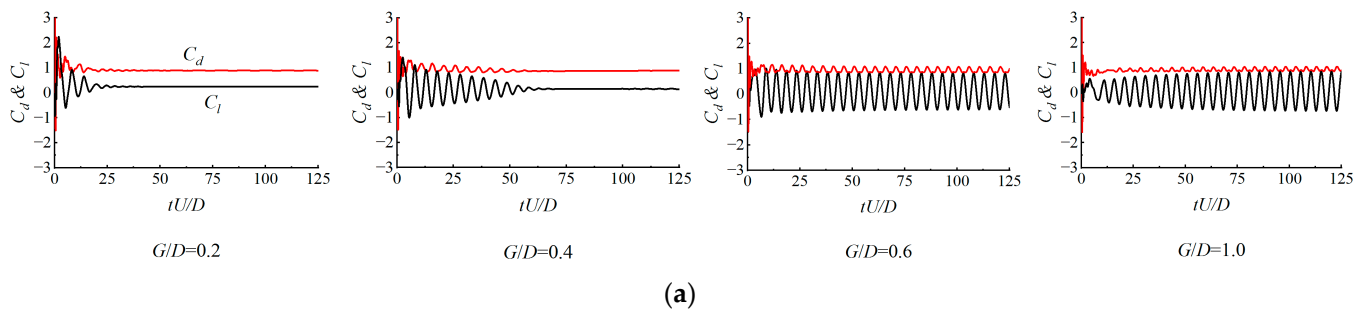


Figure 7. Cont.

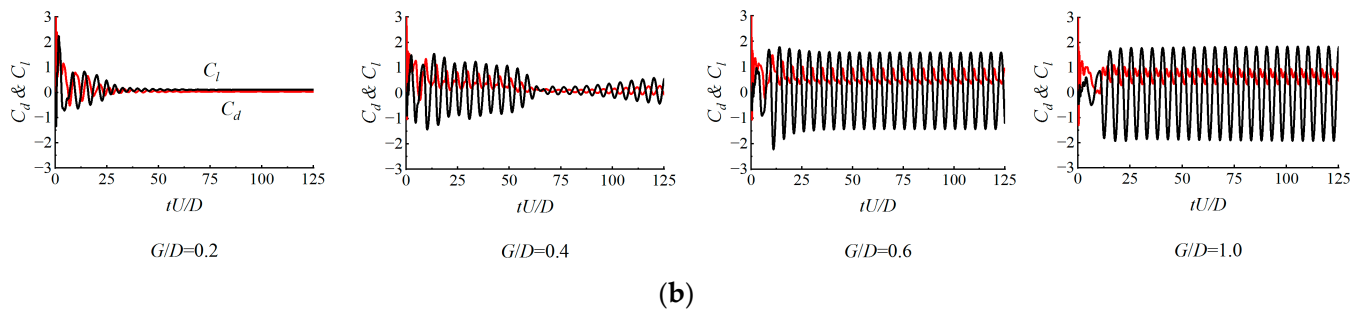


Figure 7. Time history of the drag and lift coefficient on two tandem cylinders at $Re = 6300$ for $T/D = 3$: (a) the upstream cylinder; and (b) the downstream cylinder.

The flow between the two cylinders becomes unstable for $G/D < 0.6$ due to the interference of the upstream cylinder and the adjacent wall, as seen in Figures 6 and 7. The shear layer of the upstream cylinder adheres to the front surface of the downstream one, affecting the force coefficient on the downstream cylinder. For $G/D \geq 0.6$, the wall effect is weakened, and the two cylinders exhibit periodical force variation.

Figure 8 demonstrates the average force coefficients of \bar{C}_d and \bar{C}_l on two near-wall tandem cylinders. The \bar{C}_d on the downstream cylinder is smaller than that on the upstream one at different G/D due to the sheltering effects of the upstream cylinder. For the upstream cylinder, \bar{C}_d and \bar{C}_l are close to those on the near-wall single cylinder, indicating that the wall imposes significant effects on the upstream cylinder. For the downstream cylinder, \bar{C}_d is smaller than that on the upstream cylinder. This is because the shear layer of the upstream cylinder extends or adheres to the front surface of the downstream cylinder, reducing the impact on the downstream cylinder. When the wall effect is weakened ($G/D > 0.6$), the \bar{C}_l increases as the T/D grows. The possible reason for this is that the downstream cylinder exerts the regular and stable vibration, and the intensity of vortex shedding increases when the influence of the upstream cylinder is weakened.

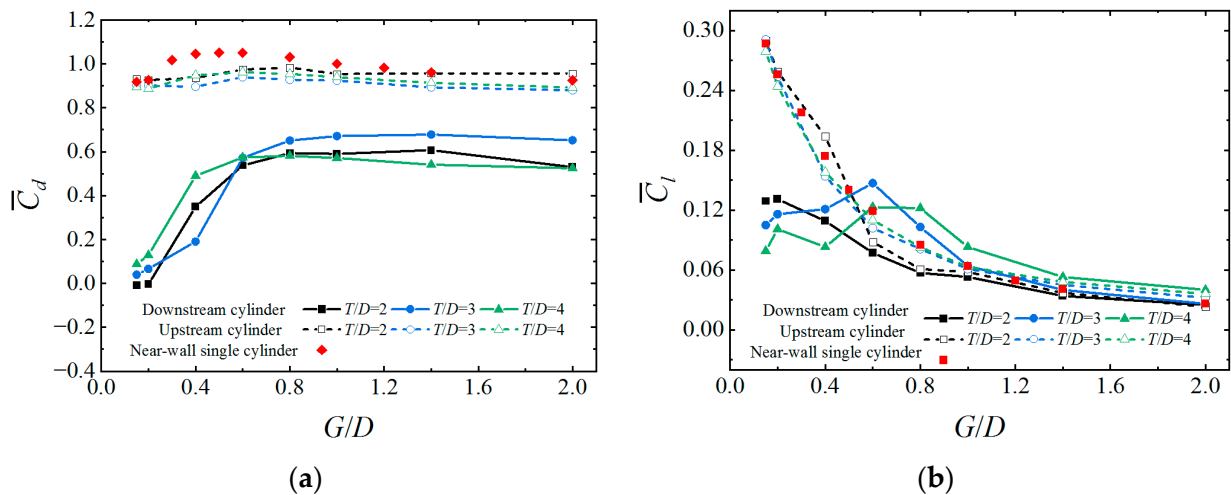


Figure 8. The average drag and lift coefficients of \bar{C}_d and \bar{C}_l on two tandem near-wall cylinders at $Re = 6300$ for different T/D : (a) average drag coefficient; and (b) average lift coefficient.

The spectrum of C_l on two cylinders by fast Fourier transform (FFT) for $G/D = 2$ and 1.4 at three T/D is shown in Figure 9. At $G/D = 2$, multiple peaks of the C_l spectrum appear, indicating that the vortex-shedding frequency is unstable. It is shown in Figure 6 that unstable vortex shedding occurs initially and is then suppressed after several cycles. For $G/D = 1.4$, there is only a single peak, indicating that the vortex-shedding frequency is relatively stable. As the T/D rises, the vortex-shedding frequency rises. Meanwhile, the vortex-shedding frequencies and the peaks of the C_l spectrum on both cylinders are

basically the same for a given G/D and T/D . This reveals that the near-wall effect and the interaction characteristics of the two cylinders have a more remarkable influence on two cylinders as a whole, while they have less influence on the individual ones.

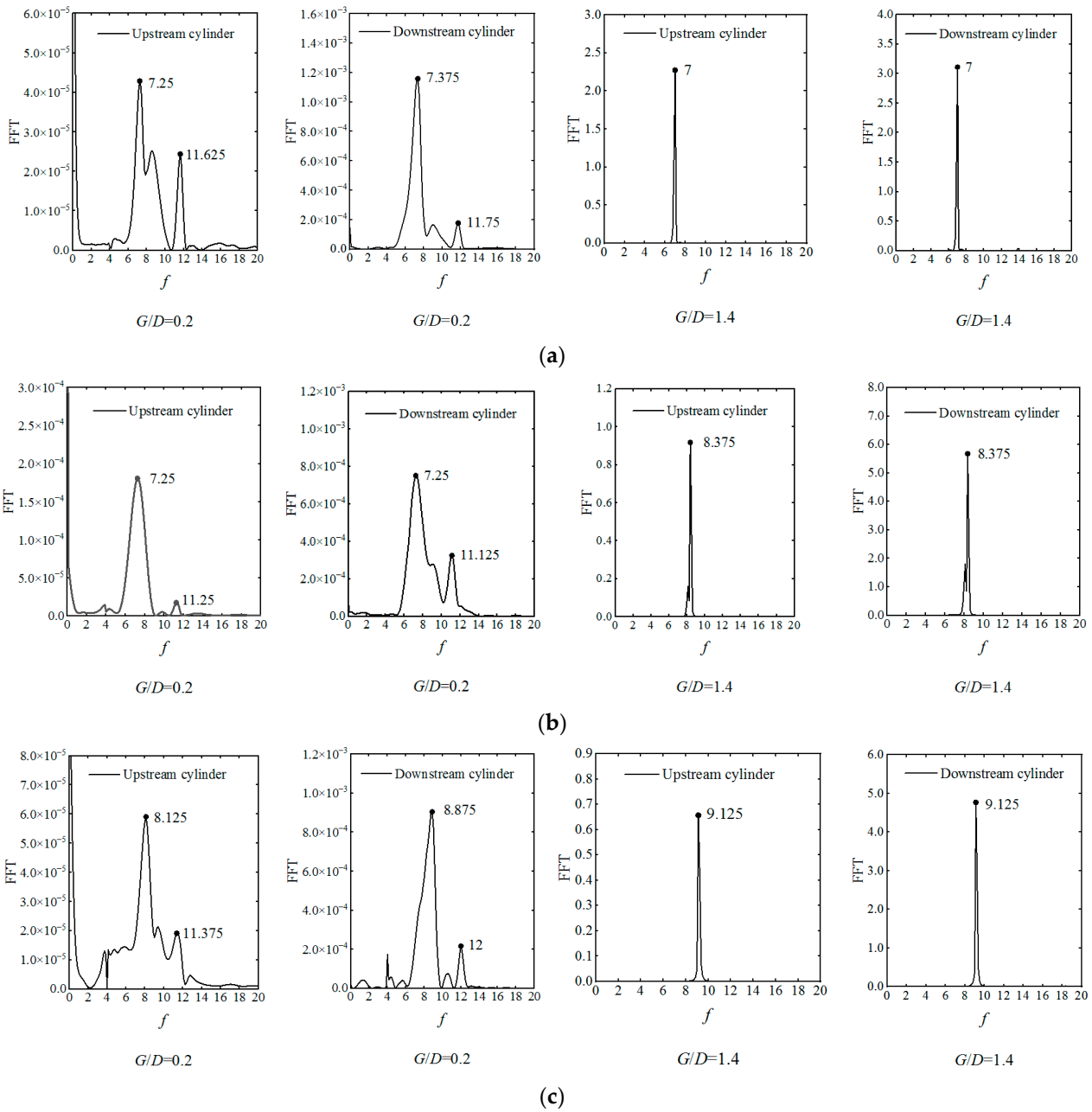


Figure 9. Spectrum of C_l on two tandem near-wall cylinders at $Re = 6300$ for $G/D = 2$ and 1.4 at three T/D : (a) $T/D = 2$; (b) $T/D = 3$; and (c) $T/D = 4$.

To reveal the interaction mechanism, the horizontal and vertical velocities at several typical positions for $T/D = 3$ are investigated, as shown in Figure 10. The positions of $X1$ and $X2$ are located at a horizontal distance of D and $2D$ away from the center of the upstream cylinder, respectively. Also, $X3$ is $2D$ away from the center of the downstream cylinder. To reproduce the flow details, the velocity profiles of the local area around the cylinder at positions of $X1$ – $X3$ are presented.

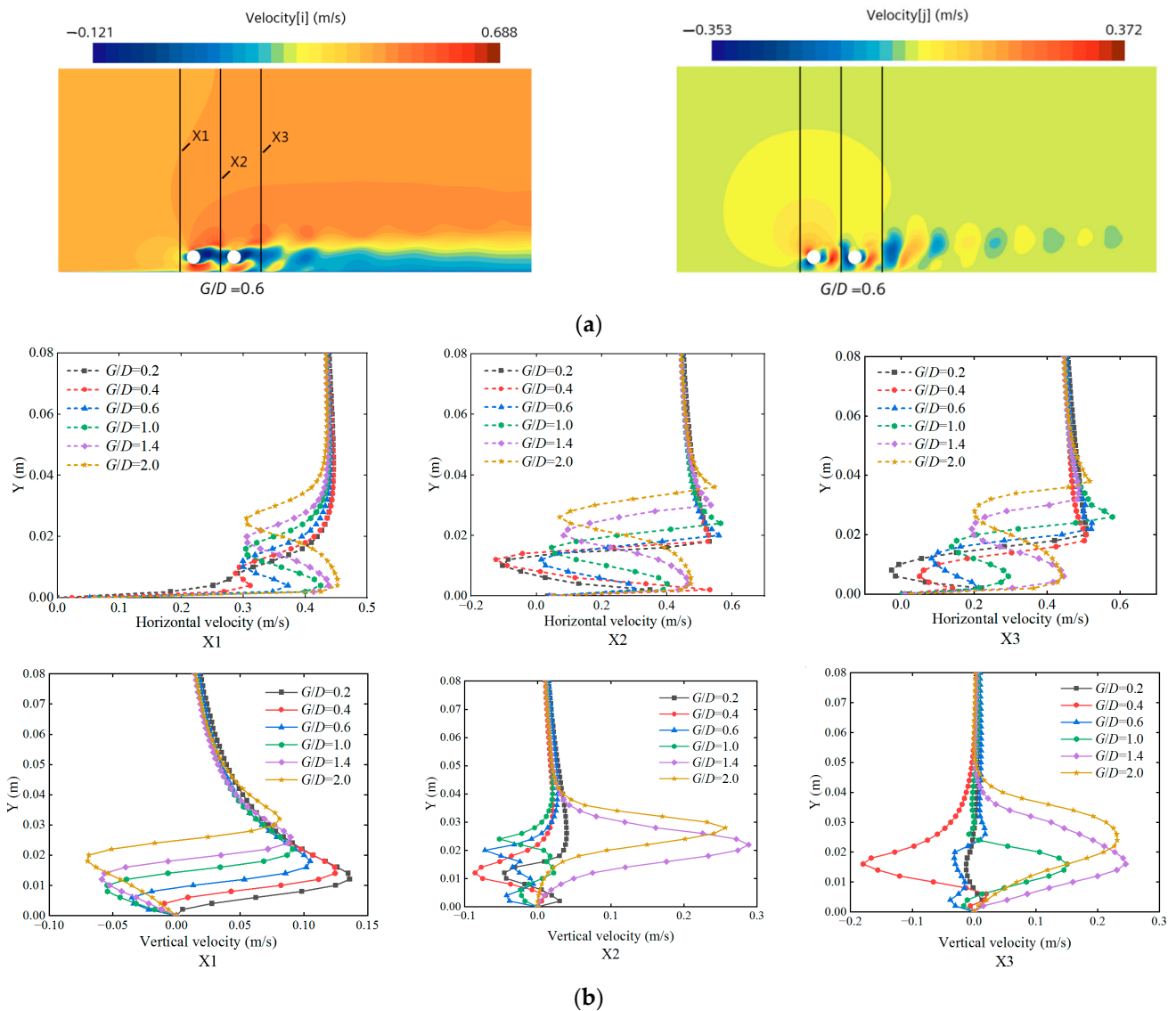


Figure 10. Horizontal and vertical velocities at several typical positions at $Re = 6300$ for $T/D = 3$: (a) contours of the horizontal and vertical velocities; and (b) vertical profiles of the horizontal and vertical velocities for different G/D .

In Figure 10a, the horizontal velocity of the incoming flow is reduced when it reaches the front side of the cylinder. It rises sharply on two sides of the cylinder. The horizontal velocity forms a deceleration band behind the cylinder and extends downstream. Meanwhile, a pair of periodic positive and negative vortices is generated behind the cylinder when the vertical velocity encounters the obstruction of the cylinder. They dissipate slowly when moving downstream. In Figure 10b, the positive peak of the vertical velocity slowly reduces and transients to the negative one as the G/D increases before the incoming flow velocity encounters the upstream cylinder. However, the maximum horizontal velocity does not change much.

In detail, for $G/D \leq 0.2$, the horizontal velocity at the gap decreases continuously to 0, which explains the moderate changes in the pressure coefficient for $G/D \leq 0.2$ in Figure 5. At the X2 position, the peak of the vertical velocity becomes larger as G/D decreases. This indicates that the existence of the wall affects the intensity of the periodic positive and negative vortices. However, the trough value of the horizontal velocity returns to a constant value (about 0.06 m/s) as the G/D increases.

For $G/D = 2$, the horizontal velocity at the gap has a back-flow region. The peak of the vertical velocity changes chaotically behind the downstream cylinder (X3 position). The trough peak of the horizontal velocity returns to a constant value (about 0.2 m/s) as the G/D rises. The peak of the horizontal velocity at the X2 position is lower than that at the X3 position for the same G/D . The reason for this is that the horizontal velocity decreases when it hits the upstream cylinder. The horizontal velocity reduces further due to the interference of the downstream cylinder.

The variation of St with T/D and G/D on the downstream cylinder is shown in Figure 11. The St obviously increases with the increase in T/D for the same G/D . It is smaller than that of the single cylinder near the wall, because the gap flow between the two cylinders hinders the generation of the vortex shedding. As the G/D increases, the hydrodynamic interference between the two cylinders is weakened, and thus the frequency characteristics of the downstream cylinder approach those of the single near-wall cylinder. For $G/D > 0.6$, the change in St is small since the wall has negligible effects on the vortex-shedding frequency of the cylinder. Consequently, the downstream cylinder exhibits the sinusoidal oscillation variation.

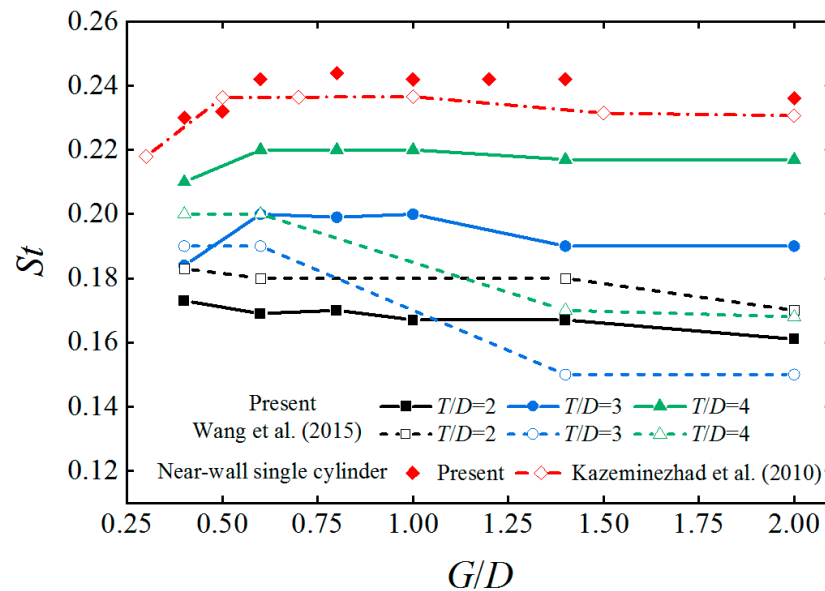


Figure 11. The variation of the St number with T/D and G/D for the downstream cylinder and near-wall single cylinders at $Re = 6300$ [40,42].

4.3. Two Near-Wall Parallel Cylinders

In this section, the flows around two parallel cylinders near a wall under different G/D and T/D at $Re = 6300$ are discussed. The local vorticity contours around two parallel cylinders are first investigated, as shown in Figure 12. In the case of $T/D = 1.5$, the shear layers of the two cylinders are in an extended state at $G/D = 0.2$. The vortices are suppressed, showing a double-stretching mode. As the gap ratio grows to $G/D = 0.4$, the vortices on the two cylinders reappear after being suppressed. The oscillation amplitude of the lower cylinder is higher than that of the upper one, which reflects the different intensity of vortex shedding. In addition, the vortex pattern in Figure 12 shows a hetero-vortex scale mode, where the vortex structure of the upper cylinder is larger than that of the lower one. This is because the wake flow deflects to one side, leading to the asymmetric vortex size of the two cylinders. For $G/D = 0.6$, the unstable vortex shedding is inhibited again. The wake size of the two cylinders is enlarged for $G/D = 1.0$, since the wall effect and the deflection of the gap flow are weakened.

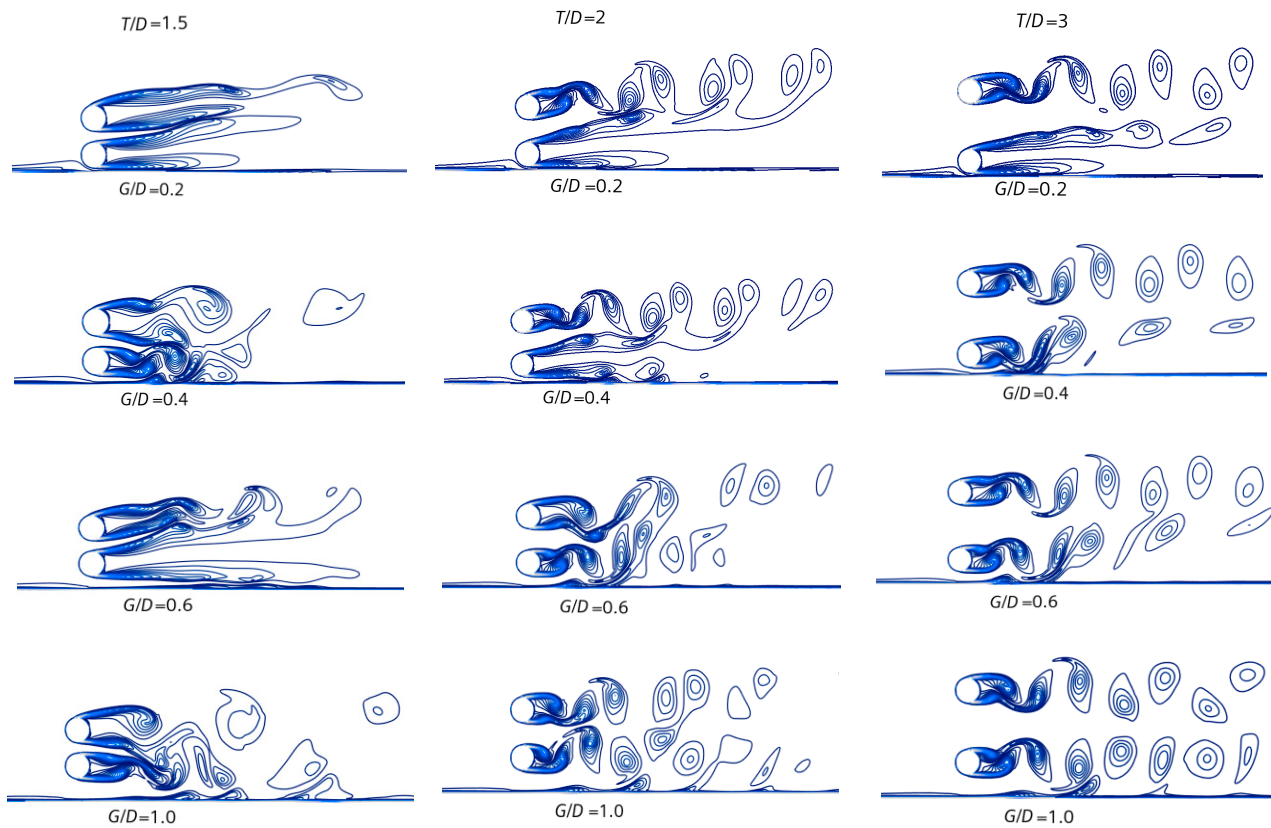


Figure 12. Instantaneous vorticity contours around the two near-wall parallel cylinders at $Re = 6300$ for different G/D and T/D .

When T/D is 2.0, the wake exhibits a unilateral vortex mode for $G/D \leq 0.4$, where alternative vortex shedding from the upper cylinder is generated, and that from the lower cylinder is inhibited. As the gap ratio grows to $G/D \geq 0.6$, both cylinders form complete vortex shedding. In comparison with that in the case of $T/D = 1.5$, the amplitude of the wake changes slightly, which indicates that the deflection phenomenon of the gap flow is not obvious.

For $T/D = 3.0$, the shedding vortices on the two cylinders can be clearly distinguished at $G/D \geq 0.4$. In this situation, the hydrodynamic interference between the two cylinders is weakened, and the deflection phenomenon of the gap flow disappears. The wake pattern is similar with that of the near-wall single cylinder, showing a free vortex mode. Meanwhile, there are two opposite states of the two cylinders: the hetero-vortex scale mode or free vortex mode in Figure 12. For $G/D \leq 0.6$, the vortex shedding shows a synchronous in-phase state, where the shear layers of the two cylinders are shed simultaneously. In contrast, the vortex shedding shows a synchronous out-of-phase state for $G/D = 1.0$.

The time histories of the lift coefficient C_l and the drag coefficient C_d on two cylinders at $T/D = 1.5$ are presented in Figure 13. Correspondingly, Figure 14 demonstrates the average drag and lift coefficients of \bar{C}_d and \bar{C}_l on two parallel cylinders. If $G/D \leq 0.6$, the \bar{C}_d on the two cylinders shows a distinct pattern for different T/D . As G/D is larger than 0.6, the \bar{C}_d of the two cylinders shows the similar variation trend. The \bar{C}_d decreases with the increase in T/D , since the wall effect is dominant when the gap ratio is small. On the other hand, the wake interaction between the two cylinders plays the dominant role when the gap ratio is larger than a critical value. Also, the wake interaction becomes weak with the increase in the gap ratio.

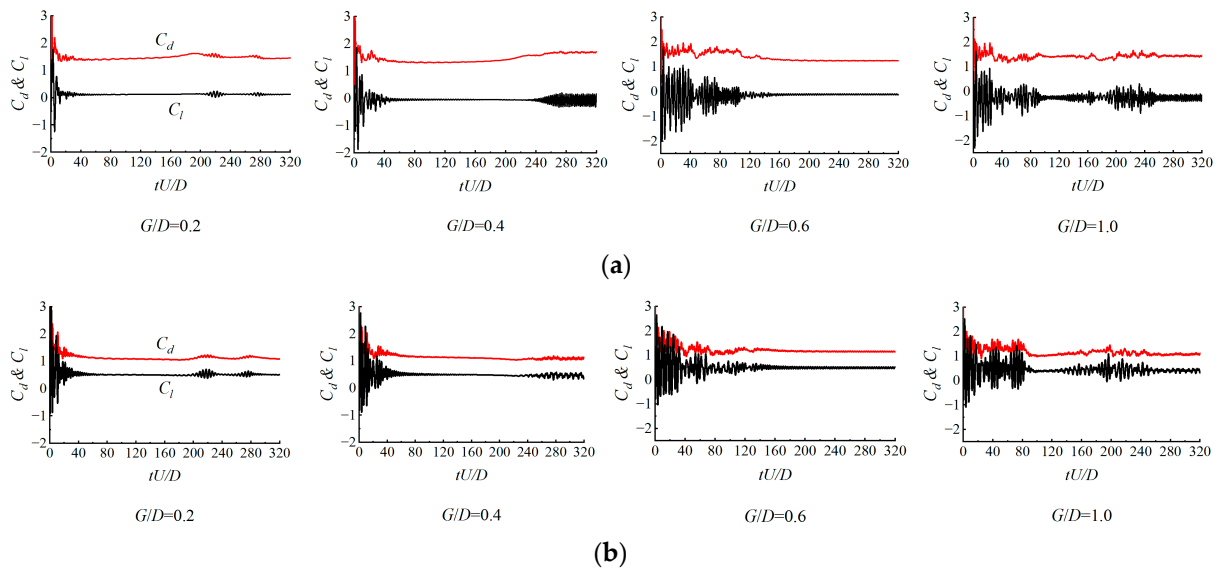


Figure 13. Time history of C_d and C_l on two near-wall parallel cylinders at $Re = 6300$ for $T/D = 1.5$: (a) the lower cylinder; and (b) the upper cylinder.

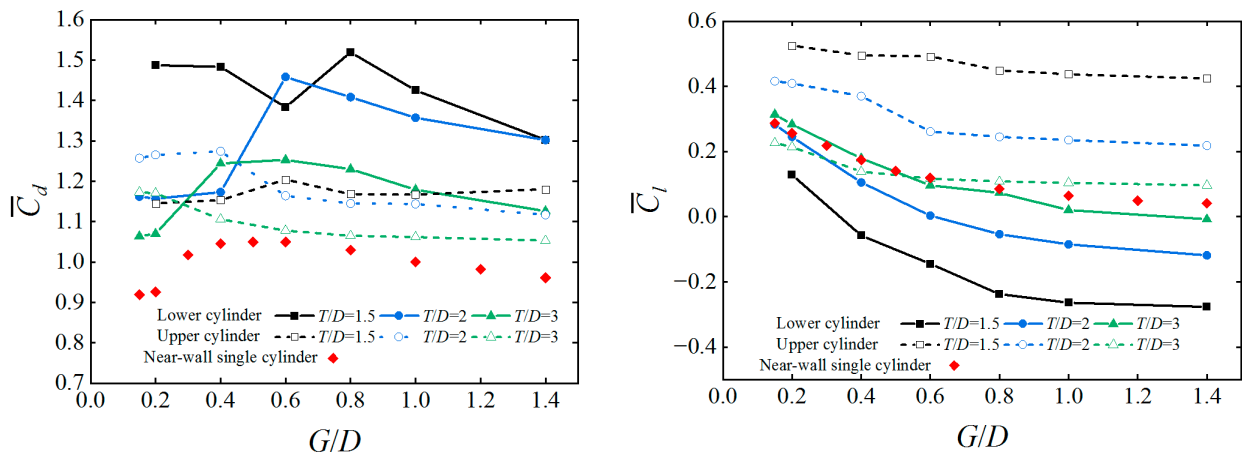


Figure 14. The average drag and lift coefficients of \bar{C}_d and \bar{C}_l on two parallel cylinders near the wall at $Re = 6300$ for different T/D .

It is seen in Figure 14 that the \bar{C}_l on two cylinders reduces with the increase of the G/D . However, the two cylinders show opposite trends as the T/D grows. The \bar{C}_l on the upper cylinder decreases, and that on the lower cylinder increases as the T/D decreases. This is because the gap flow has an outward repulsion effect. The repulsion effect is weakened, and the \bar{C}_l on the two cylinders is consistent with that in the single cylinder case as the spacing ratio increases.

The spectrum of C_l on two parallel cylinders by FFT for $G/D = 2$ and 1.4 at three T/D is demonstrated in Figure 15. For $T/D = 1.5$, there is no obvious peak in the spectrum. According to Figure 12, it is observed that the unstable vortex shedding of the two cylinders is restrained. For $T/D = 2$, there is a single peak, and the frequencies of the two cylinders are identical at $G/D = 2$. The upper cylinder exhibits stable vortex shedding, while that of the lower cylinder is restrained. However, the shedding vortices of the two cylinders can interact with each other due to the small spacing, resulting in the identical frequencies. For the case of $G/D = 1.4$, there are two peaks, and the main peaks of the two cylinders are different. The reason for this is that the gap flow is inclined to one side of the cylinder, leading to different vortex-shedding frequencies.

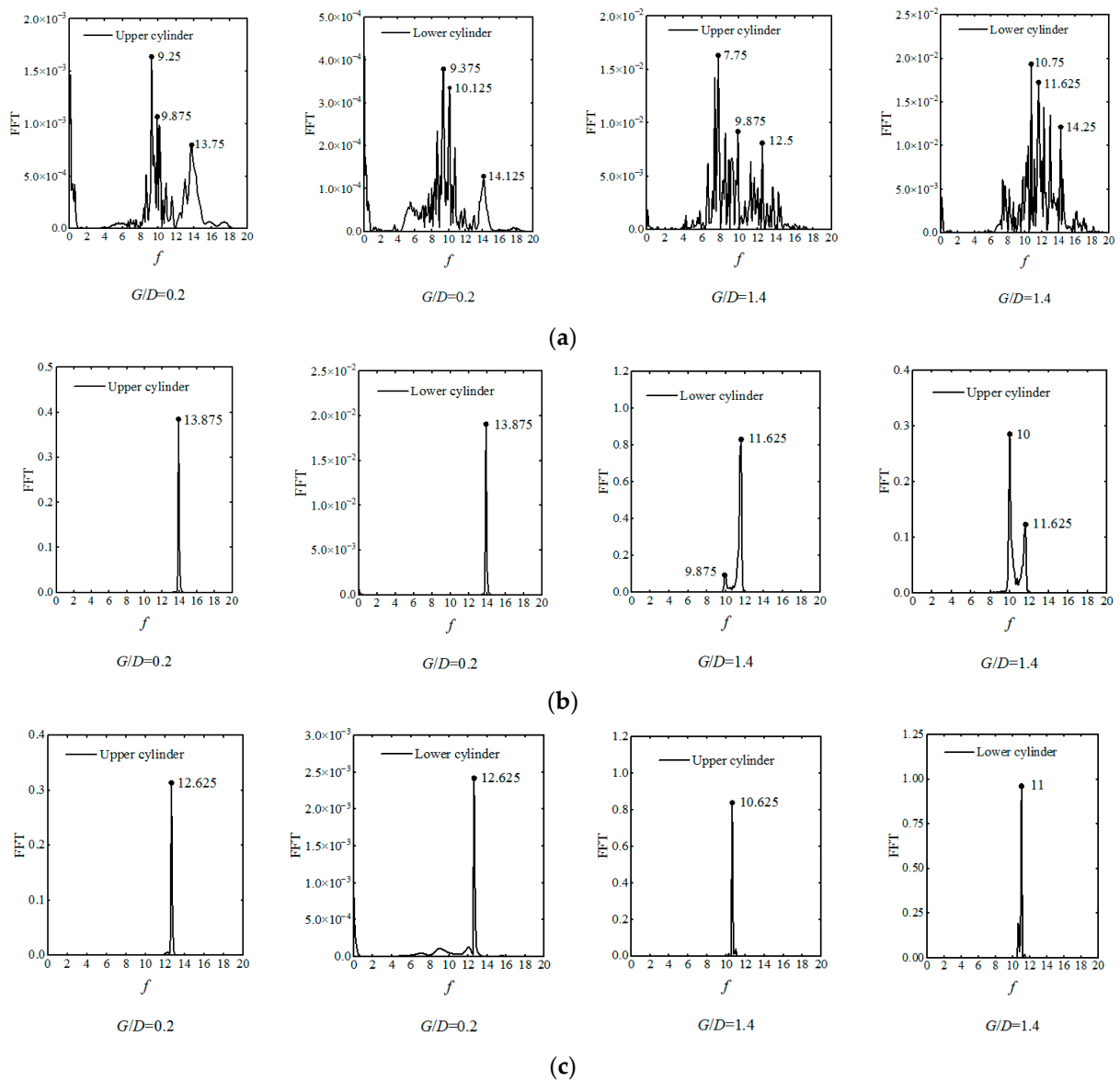


Figure 15. Spectrum of C_1 on two near-wall cylinders at $Re = 6300$ for $G/D = 2$ and 1.4 at three T/D : (a) $T/D = 1.5$; (b) $T/D = 2$; and (c) $T/D = 3$.

For $T/D = 3$, a single peak exists, and two cylinders have the identical frequencies at $G/D = 2$. When $G/D = 1.4$, it is still a single peak, while the frequencies of the two cylinders are slightly distinct. The reason for this is that the deflection phenomenon of the gap flow and the mutual interference effect between the two cylinders are weakened as the spacing ratio increases. Consequently, the stable vortex shedding of both cylinders is formed, and the hydrodynamic interference between the two cylinders can be negligible. Meanwhile, the vortex-shedding frequency of the two cylinders is reduced as the T/D increases, indicating that the intensity of vortex shedding is weakened.

Figure 16 shows the local profiles of the horizontal and vertical velocities at a typical location, where $X4$ is located $2D$ from the cylindrical center. In Figure 16a, a clear deflection of the gap flow can be observed, resulting in a narrower and wider jet of the horizontal velocity behind the two cylinders, respectively. The vertical velocity has periodic positive and negative velocity vortices on the upper cylinder, while the velocity contours at the lower cylinder are inhibited.

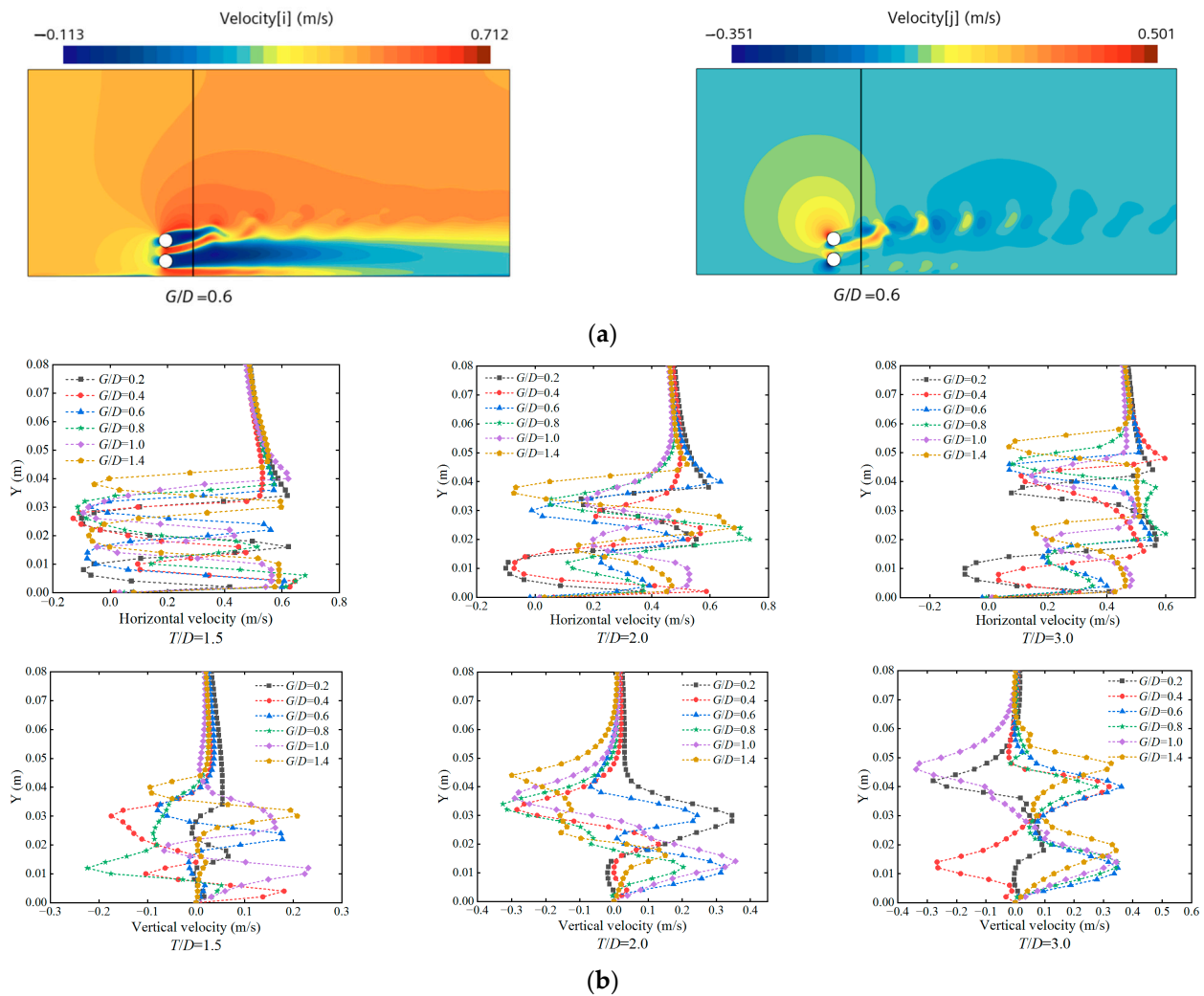


Figure 16. Vertical profiles of the horizontal and vertical velocities at typical locations at $Re = 6300$: (a) velocity contours for $T/D = 1.5$ and $G/D = 0.6$; and (b) variation of horizontal and vertical velocities with G/D and T/D .

For $T/D = 1.5$, the hydrodynamic interference characteristics between the two cylinders are strong, as shown in Figure 16b. The trough values of the horizontal velocity behind the two cylinders are basically equal, while the peak values of the vertical velocity change in a disordered fashion. For $T/D = 2.0$, the hydrodynamic interference between the two cylinders is weakened, and the horizontal velocity behind the two cylinders has different peaks. If G/D is small, the velocity peak behind the lower cylinder is lower. The velocity peak behind the upper cylinder is reduced as the G/D increases. However, the wake flow of the lower cylinder begins to break away from the inhibition state, and the intensity of the velocity vortex is increased. In the case of $T/D = 3.0$, the peak value of the horizontal velocity behind the upper cylinder does not change with the G/D . Also, the maximum horizontal velocity behind the lower cylinder recovers to a constant value as the G/D grows. The maximum vertical velocity behind the two cylinders has two states: the same side ($G/D = 0.6, 0.8, 1.4$) and the opposite side ($G/D = 0.4, 1.0$). This indicates that the periodic velocity vortices show synchronous in-phase and synchronous out-of-phase states. For the same G/D , the maximum horizontal velocity behind the lower cylinder changes little as the T/D increases.

The Strouhal number St as a function of the T/D and G/D on the lower cylinder is demonstrated in Figure 17. The change in the St is small for $G/D > 0.6$. For the same G/D , the Strouhal number St of the lower cylinder is reduced as the T/D increases and

approaches that seen in the case of the near-wall single cylinder. This results from the fact that the near-wall effect and the hydrodynamic interference make the wake unstable when the T/D is small and thus affects the vortex-shedding frequency. However, the near-wall effect and the hydrodynamic interference are weakened as the T/D further increases. It is observed that the wake pattern of the two cylinders is similar with that in the single cylinder case.

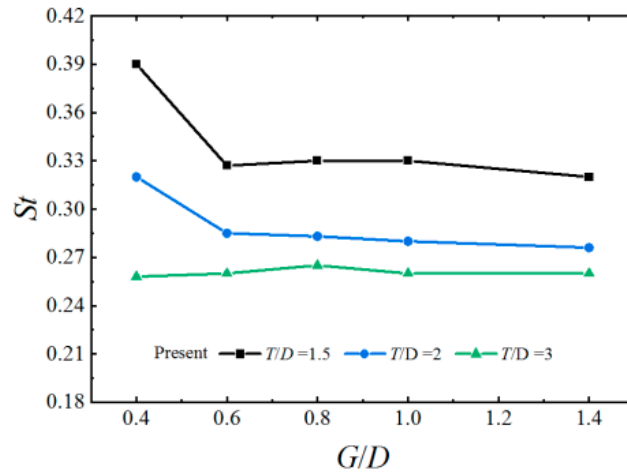


Figure 17. The variation of St with T/D and G/D at $Re = 6300$ for the parallel lower cylinder near the wall.

5. Conclusions

The 2D flows around a single cylinder, two tandem, and two parallel cylinders near a wall have been studied in this paper using the software of STAR CCM+. The accuracy of the present model is demonstrated in comparison with the experimental [40,41,43] and other numerical [42,44,45] results. Good grid convergence has been achieved. Note that Lei et al. [41] and Kazeminezhad et al. [42] only focused on the near-wall effects on a single cylinder. Wang et al. [43] investigated the flows around the near-wall for tandem two cylinders and found three types of vortex-shedding modes. However, comprehensive results were not obtained, including the fluid details and the force coefficients. In this work, the wake patterns, the force coefficients, and vortex-shedding frequencies under different gap distances and cylinders spacing are investigated. The influence of the wall effect and the hydrodynamic interference between two cylinders are explored. The main conclusions are as follows.

For flows around a single cylinder near the wall, the critical gap of $G/D = 0.6$ is identified. For $G/D < 0.6$, the wall can impose apparent effects on the force coefficient and wake structures. In particular, the vortex shedding is completely inhibited for $G/D \leq 0.2$. However, the vortex pattern near the wall transients from the suppressed state to the independent vortex-shedding state as the G/D increases. The position, where the wall vortex appears, will move backward until $G/D > 0.6$, and then the wall vortex disappears. The wall effects can be negligible for $G/D > 0.6$.

For the flows around two tandem cylinders near the wall, the wake shows three states: a stretching mode at $T/D = 1.5$, an attachment mode at $T/D = 3$, and an impinging mode at $T/D = 4$. The force coefficient on the upper cylinder is similar to that on the single cylinder near the wall. The force coefficient on the downstream cylinder is mainly affected by the upstream cylinder. However, the force coefficient on the two cylinders exhibits a similar variation trend, where both the \bar{C}_d and \bar{C}_l are gradually reduced as the G/D further increases. It is observed that the \bar{C}_d on the downstream cylinder is smaller than that on the upstream one, since the incoming flow toward the downstream cylinder is blocked by the upstream one. In addition, the Strouhal number on the downstream cylinder near the wall

grows with the increase in the T/D . It is smaller than that in the near-wall single cylinder case, since the existence of the upstream cylinder inhibits the vortex shedding at the gap.

For the flows around two near-wall parallel cylinders, the wake shows four modes: (1) a double-stretching mode for a small T/D and G/D ; (2) a hetero-vortex scale mode when T/D is small and G/D is large; (3) a unilateral vortex mode for T/D being large and G/D being small; (4) a free vortex mode if T/D and G/D are both large. Moreover, the hetero-vortex scale mode or free vortex mode exhibits two states: synchronous in-phase state and synchronous out-of-phase state. The force coefficients on both cylinders are remarkably influenced by the wall effects for $G/D \leq 0.6$. For $G/D > 0.6$, the \overline{C}_d on both cylinders decreases as the T/D increases, and the \overline{C}_l exhibits the opposite variation trend. The \overline{C}_d on both cylinders approaches that on the near-wall single cylinder. The \overline{C}_l on the upper cylinder decreases from 0.5 to 0.15, and that on the lower cylinder increases from -0.3 to 0.06.

The present study focuses on 2D simulation to save computational resources. However, the three-dimensional (3D) turbulent effects of the wake cannot be ignored for a large Reynolds number. To investigate the 3D effects, we intend to simulate the 3D flows around near-wall circular cylinders with different aspect ratios in the near future.

Author Contributions: Conceptualization, J.X.; methodology, X.C. and P.Y.; software, P.Y.; formal analysis, X.C.; investigation, J.X.; resources, L.W.; writing—original draft preparation, X.C.; writing—review and editing, J.X.; visualization, F.S.; funding acquisition, J.X. and F.S. All authors have read and agreed to the published version of the manuscript.

Funding: This research was funded by the National Science Foundation of China (NO. 51909124), Natural Science Foundation of Zhejiang Province, China (NO. 11LY21E090001), State Key Laboratory of Maritime Technology and Safety, Scientific and Technological Program of Chongqing Municipal Education Commission for Youths (NO. KJQN202100704), and 2022 Chongqing Science and Technology Bureau ‘Doctoral Through Train’ Project (NO. CSTB2022BSXM-JCX0161).

Institutional Review Board Statement: Not applicable.

Informed Consent Statement: Not applicable.

Data Availability Statement: The original contributions presented in the study are included in the article.

Conflicts of Interest: Author Xing Chang was employed by the Company Shanghai Ship and Shipping Research Institute Co., Ltd. The remaining authors declare that the research was conducted in the absence of any commercial or financial relationships that could be construed as a potential conflict of interest.

Nomenclature

u	Cartesian velocity vector	U_0	Free-stream velocity
t	Time	θ	Angle
p	Pressure	D	Cylinder diameter
ρ	Density	St	Strouhal numbers
μ	Dynamic viscosity coefficient	f	Vortex-shedding frequency
Re	Reynolds number	F_l, F_d	Lift and drag forces on the cylinder
T	Center distance between two cylinders	G	Distance from the lower surface of a cylinder to the wall
k	Turbulent kinetic energy	ε	Turbulent dissipation rate
μ_t	Turbulent viscosity coefficient	\overline{C}_d	Average drag coefficient
C_d	Drag coefficient	\overline{C}_l	Average lift coefficient
C_l	Lift coefficient	x_i ($i = 1, 2$)	Coordinates in the x- and y-directions
δ_{ij}	Kronecker delta function		

References

1. Wang, C.X. Research on Vortex Shedding and Hydrodynamic Characteristics of a Near-plane Circular Cylinder. Ph.D. Thesis, Harbin Engineering University, Harbin, China, 2016.
2. Zhang, Z.M. Three-Dimensional Numerical Simulations on Flow Pasting a Stationary and Vibrating Cylinder Near a Wall with Different Attack Angles. Master's Thesis, Tianjin University, Tianjin, China, 2018.
3. Wang, L.; Lei, L.; Ma, T.; Zheng, K.; Guo, J. Investigation on the flow-induced vibration of tandem cylinders with varying diameters at subcritical Reynolds numbers. *Appl. Ocean Res.* **2023**, *138*, 103669. [[CrossRef](#)]
4. Aksoy, M.H. Flow characteristics and passive flow control of circular cylinders with triangular vortex generators: An experimental investigation. *Appl. Ocean Res.* **2024**, *142*, 103836. [[CrossRef](#)]
5. Misuriya, G.; Eldho, T.I.; Mazumder, B.S. Experimental investigations of turbulent flow characteristics around different cylindrical objects using PIV measurements. *Eur. J. Mech. B. Fluid.* **2023**, *101*, 30–41. [[CrossRef](#)]
6. Amini, Y.; Izadpanah, E.; Zeinali, M. A comprehensive study on the power-law fluid flow around and through a porous cylinder with different aspect ratios. *Ocean Eng.* **2024**, *296*, 117035. [[CrossRef](#)]
7. Dynnikova, G.Y. Simulation of two-dimensional flow around an elliptical cylinder at high Reynolds numbers. *Phys. Fluid.* **2024**, *36*, 023109. [[CrossRef](#)]
8. Duan, M.; Wan, D. Large eddy simulation of three-dimensional cylindrical flow around 3900. *J. Ocean Eng.* **2016**, *34*, 11–20.
9. Manzoor, R.; Mushtaq, S.; Nadeem, N.; Perveen, S.; Kalsoom, S.; Naeem, A.; Akbar, R. Numerical investigation of flow past a triangular cylinder at various Reynolds numbers. *Phys. Fluid.* **2023**, *35*, 124101. [[CrossRef](#)]
10. Aksoy, M.H.; Goktepe, I.; Ispir, M.; Cakan, A. Machine Learning Approach for Flow Fields Over a Circular Cylinder Based on Particle Image Velocimetry Measurements. *Ocean Eng.* **2023**, *223*, 113699. [[CrossRef](#)]
11. Lam, K.; Li, J.Y.; Chan, K.T.; So, R.M.C. Flow pattern and velocity field distribution of cross-flow around four cylinders in a square configuration at a low Reynolds number. *J. Fluids Struct.* **2003**, *17*, 665–679. [[CrossRef](#)]
12. Niegodajew, P.; Gajewska, K.; Elsner, W.; Gnatowska, R. Experimental investigation of flow characteristics around tandem arrangement of triangular and square cylinders. *J. Fluid Struct.* **2024**, *124*, 104045. [[CrossRef](#)]
13. Mishra, S.K.; Sen, S. On the critical spacing between two in-line diamond cylinders at $Re = 100$. *Ocean Eng.* **2024**, *296*, 117011. [[CrossRef](#)]
14. Mashhadi, A.; Sohankar, A.; Alam, M.M. Flow over rectangular cylinder: Effects of cylinder aspect ratio and Reynolds number. *Int. J. Mech. Sci.* **2021**, *195*, 106264. [[CrossRef](#)]
15. Shuzheng Sun, S.Z.; Yang, W.Q.; Liu, S.N.; Li, P.; Ong, M.C. Computational fluid dynamics simulations of a near-wall rectangular cylinder in an oscillatory flow. *Ocean Eng.* **2024**, *304*, 117776.
16. Chen, N.; Zhang, R.G.; Liu, Q.S.; Ding, Z.D. Deep reinforcement learning-based active control for drag reduction of three equilateral-triangular circular cylinders. *Eur. J. Mech. B. Fluid.* **2024**, *104*, 114–122. [[CrossRef](#)]
17. Tu, J.H.; Yu, L.H.; Gang, H.; Wang, G.Y. Flow characteristics and mechanism of three cylinders in a triangular arrangement. *J. Ship Mech.* **2024**, *28*, 354–367.
18. Tu, J.; Zhang, Z.; Lv, H.; Han, Z.; Fu, S. Influence of the center cylinder on the flow characteristics of four-and five-cylinder arrays at subcritical Reynolds number. *Ocean Eng.* **2020**, *218*, 108245. [[CrossRef](#)]
19. Sarpkaya, T. A critical review of the intrinsic nature of vortex-induced vibrations. *J. Fluids Struct.* **2004**, *19*, 389–447. [[CrossRef](#)]
20. Gabbai, R.D.; Benaroya, H. An overview of modeling and experiments of vortex-induced vibration of circular cylinders. *J. Sound Vib.* **2005**, *282*, 575–616. [[CrossRef](#)]
21. Williamson, C.; Govardhan, R. A brief review of recent results in vortex-induced vibrations. *J. Wind Eng. Ind. Aerod.* **2008**, *96*, 713–735. [[CrossRef](#)]
22. Sumner, D. Two circular cylinders in cross-flow: A review. *J. Fluid. Struct.* **2010**, *26*, 849–899. [[CrossRef](#)]
23. Wu, X.; Fei, G.; Hong, Y. A review of recent studies on vortex-induced vibrations of long slender cylinders. *J. Fluids Struct.* **2012**, *28*, 292–308. [[CrossRef](#)]
24. Zhou, Y.; Alam, M.M. Wake of two interacting circular cylinders: A review. *Int. J. Heat Fluid Flow* **2016**, *62*, 510–537. [[CrossRef](#)]
25. Chen, W.M.; Fu, Y.Q.; Guo, S.X.; Jiang, C.H. Fluid-solid coupling and dynamic response of vortex induced vibration of slender ocean cylinders. *Adv. Mech.* **2017**, *47*, 201702.
26. Wang, J.S.; Fan, D.; Lin, K. A review on flow-induced vibration of offshore circular cylinders. *J. Hydrodyn. B.* **2020**, *32*, 415–440. [[CrossRef](#)]
27. Ouro, P.; Muhawanimana, V.; Wilson, C.A.M.E. Asymmetric wake of a horizontal cylinder in close proximity to a solid boundary for Reynolds numbers in the subcritical turbulence regime. *Phy. Rev. Fluids.* **2019**, *4*, 104604. [[CrossRef](#)]
28. Zhou, L.; Xu, H.; Xi, G. Experimental study on PIV on the influence of gap ratio on the flow around a single cylinder near the wall. *J. Mech. Des. Fabr.* **2020**, *11*, 21–25.
29. Zhang, Z.; Ji, C.; Xu, D. Temporal and spatial evolution of vortex shedding for flow around a cylinder close to a wall. *Ocean Eng.* **2021**, *228*, 108964. [[CrossRef](#)]
30. Zhou, J.; Qiu, X.; Li, J.; Liu, Y. Vortex evolution of flow past the near-wall circular cylinder immersed in a flat-plate turbulent boundary layer. *Ocean Eng.* **2022**, *260*, 112011. [[CrossRef](#)]
31. Zhai, S.; Ma, S.; Yin, G.; Xi, G. Experimental study of the flow characteristics of the transition flow down near-wall insertion cylinder. *J. Mech. Des. Manuf.* **2022**, *10*, 11–18.

32. Li, Z.; Li, J.; Wu, J.; Chong, K.; Wang, B.; Zhou, Q.; Liu, Y. Numerical simulation of flow instability induced by a fixed cylinder placed near a plane wall in oscillating flow. *Ocean Eng.* **2023**, *288*, 116115. [[CrossRef](#)]
33. Triyogi, Y.; Tohir, A. Numerical investigation of the flow interaction of I-type cylinder near the plane wall. *Ocean Eng.* **2022**, *253*, 111353. [[CrossRef](#)]
34. Li, M.; Wang, R.; Guo, X.; Liu, X.; Wang, L. Analysis of inflow conditions on the flow past a wall-mounted square cylinder with OpenFOAM. *Comput. Fluids* **2024**, *269*, 106120. [[CrossRef](#)]
35. Liu, Y.L.; Ding, Z.H.; Tao, Y.Z.; Qu, J.W.; Xie, X.L.; Qiu, X. Numerical study on compressible flow around a circular cylinder in proximity to the wall. *Phys. Fluid.* **2023**, *35*, 0148846.
36. Li, Z.; Abrahamsenprsic, M.; Ong, M.C.; Khoo, B.C. Large Eddy Simulations of flow around two circular cylinders in tandem in the vicinity of a plane wall at small gap ratios. *J. Fluid Struct.* **2018**, *76*, 251–271. [[CrossRef](#)]
37. Liu, Y.L.; Qi, L.M.; Zhou, J.K.; Li, J.H.; Tao, Y.Z.; Qiu, X. Experimental research on wake characteristics and vortex evolution of side-by-side circular cylinders placed near a wall. *Ocean Eng.* **2023**, *285*, 115268. [[CrossRef](#)]
38. Launder, B.E.; Spalding, D.B. The numerical computation of turbulent flow. *J. Comput. Math. Appl. Mech. Eng.* **1974**, *3*, 269–289. [[CrossRef](#)]
39. Lei, C.; Chen, L.; Armfield, S.W.; Kavanagh, K. Vortex shedding suppression for flow over a circular cylinder near a plane boundary. *Ocean Eng.* **2000**, *27*, 1109–1127. [[CrossRef](#)]
40. Wang, X.K.; Zhang, J.X.; Hao, Z.; Zhou, B.; Tan, S.K. Influence of wall proximity on flow around two tandem circular cylinders. *Ocean Eng.* **2015**, *94*, 36–50. [[CrossRef](#)]
41. Lei, C.; Cheng, L.; Kavanagh, K. Re-examination of the effect of a plane boundary on force and vortex shedding of a circular cylinder. *J. Wind Eng. Ind. Aerod.* **1999**, *80*, 263–286. [[CrossRef](#)]
42. Kazeminezhad, M.H.; Bakhtiary, A.Y.; Shahidi, A.E. Numerical investigation of boundary layer effects on vortex shedding frequency and forces acting upon marine pipeline. *J. Appl. Ocean Res.* **2010**, *32*, 460–470. [[CrossRef](#)]
43. Bearman, P.W.; Zdravkovich, M.M. Flow around a circular cylinder near a plane boundary. *J. Fluid Mech.* **1978**, *89*, 33–48. [[CrossRef](#)]
44. Zhao, M.; Cheng, L.; Teng, B. Numerical Modeling of Flow and Hydrodynamic Forces around a Piggyback Pipeline near the Seabed. *J. Waterway, Port, Coastal. Ocean Eng.* **2007**, *133*, 286–295.
45. Brørs, B. Numerical modeling of flow and scour at pipelines. *J. Hydraul. Eng.* **1999**, *125*, 511–523. [[CrossRef](#)]
46. Kravchenko, A.G.; Moin, P. Numerical studies of flow over a circular cylinder at $Re_D = 3900$. *Phys. Fluids.* **2000**, *12*, 403–417. [[CrossRef](#)]
47. Franke, J.; Frank, W. Large eddy simulation of the flow past a circular cylinder at $Re_D = 3900$. *J. Wind Eng. Ind. Aerodyn.* **2002**, *90*, 1191–1206. [[CrossRef](#)]

Disclaimer/Publisher’s Note: The statements, opinions and data contained in all publications are solely those of the individual author(s) and contributor(s) and not of MDPI and/or the editor(s). MDPI and/or the editor(s) disclaim responsibility for any injury to people or property resulting from any ideas, methods, instructions or products referred to in the content.